Matter

CellPress

Article

Ultrafast cation doping of perovskite quantum dots in flow

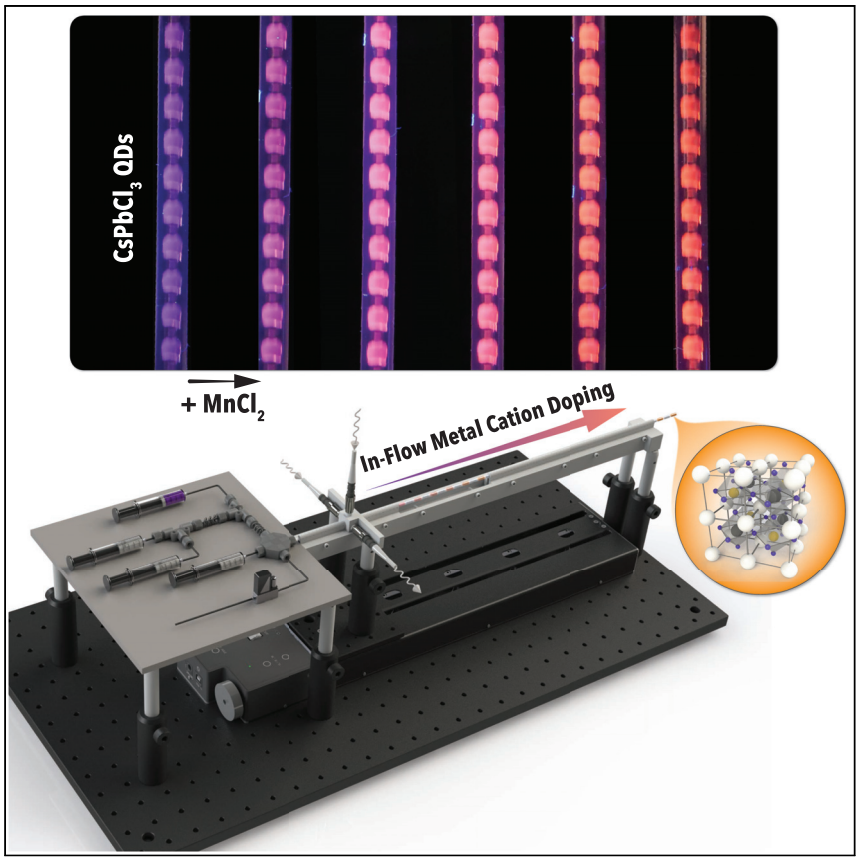

A continuous flow chemistry strategy for ultrafast metal cation doping of all-inorganic perovskite quantum dots is presented. Through accelerated in-flow studies of the metal cation-doping process, enabled by a modular microfluidic platform, a heterogeneous surface-doping mechanism is proposed.

Fazel Bateni, Robert W. Epps, Kameel Abdel-latif, ..., Tong Cai, Ou Chen, Milad Abolhasani

abolhasani@ncsu.edu

Highlights

Ultrafast continuous flow cation doping of metal halide PQDs

Microfluidic mechanistic investigations of the ultrafast cation-doping process

Unveiled a two-stage mechanism of post-synthetic cation doping of PQDs

Precise in-flow tuning of the optical properties of Mn-doped PQDs

3 **Understanding**
Dependency and conditional studies on material behavior

Bateni et al., Matter 4, 1–19
July 7, 2021 © 2021 Elsevier Inc.
https://doi.org/10.1016/j.matt.2021.04.025

Please cite this article in press as: Bateni et al., Ultrafast cation doping of perovskite quantum dots in flow, Matter (2021), https://doi.org/10.1016/j.matt.2021.04.025

Matter

CellPress

Article

Ultrafast cation doping of perovskite quantum dots in flow

Fazel Bateni,[1,3] Robert W. Epps,[1,3] Kameel Abdel-latif,[1] Rokas Dargis,[1] Suyong Han,[1] Amanda A. Volk,[1] Mahdi Ramezani,[1] Tong Cai,[2] Ou Chen,[2] and Milad Abolhasani[1,4,*]

SUMMARY

Among all-inorganic metal halide perovskite quantum dots (PQDs), cesium lead chloride ($CsPbCl_3$) with its large band-gap energy is an excellent candidate for enhancement of PQD radiative pathways through incorporation of additional internal energy transfer within its exciton band gap. In this study, we introduce a post-synthetic chemistry for ultrafast metal cation doping of $CsPbCl_3$ QDs with a high degree of tunability, using a model transition metal impurity dopant, manganese. Due to the fast nature of the post-synthetic metal cation-doping reaction, an engineered time-to-space transformation strategy is employed to unravel the kinetics and fundamental mechanism of the doping process. Using a modular microfluidic platform equipped with a translational *in situ* absorption and photoluminescence spectroscopy probe, we propose a heterogeneous surface-doping mechanism through a vacancy-assisted metal cation migration. The developed in-flow doping strategy can open new avenues for on-demand optoelectronic properties tuning and scalable precision synthesis of high-quality metal cation-doped PQDs.

INTRODUCTION

Metal halide perovskite quantum dots (PQDs) have recently emerged as a promising semiconducting material candidate with superior optical and optoelectronic properties than conventional III–V and II–VI QDs for next-generation devices.[1–8] Specifically, lead (Pb) halide PQDs have been successfully utilized in a wide range of solution-processed devices, including solar cells,[9–13] displays,[14] light-emitting diodes (LEDs),[15] biosensors,[16] lasers,[17] and photodetectors.[18,19] In addition to their defect-tolerant band-gap structure, Pb halide PQDs offer near-unity photoluminescence quantum yield (PLQY) without a secondary passivation layer, narrow emission linewidth, short radiative lifetime, negligible self-absorption, and weak PL blinking effect.[1,3,20] Moreover, due to their ionic nature and the quantum confinement effect, Pb halide PQDs possess unique size- and composition-tunable emission properties within the visible spectrum through growth rate control and post-synthesis ion exchange reactions, respectively.[21,22]

Despite the unique optoelectronic properties of Pb halide PQDs, one of the major drawbacks hindering their adoption by chemical and energy industries is the health and environmental concerns associated with the toxicity of lead.[23,24] Lead ions are instrumental for maintaining the extended lifetime and high PLQY of PQDs and the complete removal and replacement of these ions can deteriorate the structural integrity of the PQDs.[25] An alternative route based on partial cation exchange of Pb

Progress and potential

Transition metal cation-doped lead halide perovskite quantum dots (PQDs) are an emerging class of materials for next-generation photonic devices, due to their intriguing dopant-induced properties and improved photo-, moisture-, and thermal stabilities. Colloidal synthesis studies of metal cation-doped PQDs with its multifaceted nature is a challenging undertaking using conventional batch reactors. In this study, we utilize a modular microfluidic platform equipped with a mobile spectral monitoring probe to study the kinetics and unveil the chemical transformation mechanism of the ultrafast cation doping of cesium lead chloride QDs. We provide a design framework for precise tuning of the optical properties of PQDs via a post-synthetic doping mechanism in flow. The facile doping chemistry in combination with the modular microfluidic platform, developed in this work, can enable continuous nanomanufacturing of metal cation-doped PQDs with application-specific optoelectronic properties.

Please cite this article in press as: Bateni et al., Ultrafast cation doping of perovskite quantum dots in flow, Matter (2021), https://doi.org/10.1016/j.matt.2021.04.025

ions with less toxic materials that possess analogous optoelectronic properties to Pb (e.g., manganese [Mn], tin, cadmium, zinc, and bismuth) is considered as an effective strategy to mitigate the toxicity of Pb halide PQDs without sacrificing the superior optoelectronic properties and, at the same time, imparting new optical and optoelectronic properties into the pristine PQDs.[26–29] Over the past few years, Mn doping of Pb halide PQDs has been investigated as an effective route for introduction of additional magnetic and optoelectronic properties to PQDs.[30–33] Mn is the most common choice of the impurity dopant as its ionic radius and valence state resemble Pb, thereby allowing cation-exchange reactions in the lattice of the host Pb halide PQD nanocrystals.[30,31] Through Mn doping of Pb halide PQDs, the total content of Pb^{2+} ions present in the PQDs can be reduced, while adding another degree of emission tunability to the pristine nanocrystals, originating from the transfer of host excitation energy to spin polarized Mn^{2+} d-d states, resulting in a long excited-state yellow-orange emission.[33–36]

Among all-inorganic Pb halide PQDs, cesium lead chloride ($CsPbCl_3$) QDs possess the highest band-gap energy, which makes it a more favorable crystalline host for efficient energy transfer from band-edge excitons to Mn internal states. Doping $CsPbCl_3$ QDs with Mn^{2+} ions offers two distinct advantages: (1) the incorporation of Mn^{2+} ions into the PQD crystal lattice increases the tolerance factor, improves structural stability, and enhances radiative pathways,[35,37] and (2) the emission intensity of the exciton and the transition metal impurity dopants can be enhanced through the suppression of energy loss by structural defects, resulting in an increase in the PLQY of the cation-doped PQDs.[35,37]

Mn-doped Pb halide PQDs can be synthesized using one-pot, hot-injection synthesis technique, and post-synthetic cation-exchange reactions. Dual-emissive Mn-doped $CsPbCl_3$ QDs were first successfully synthesized via a colloidal one-pot, hot-injection method.[30,31] Feasibility of the post-synthetic cation exchange of Pb^{2+} with Mn^{2+} ions in $CsPbCl_3$ QDs was first studied in the work of Gao et al.[38] In this study, $CsPbCl_3$ QDs were first synthesized using a hot-injection method and used without further purification for the Mn doping with a manganese chloride ($MnCl_2$) precursor at a relatively high temperature (150°C).

Room temperature, post-synthetic metal cation doping of Pb halide PQDs can provide a higher level of control over the extent and level of doping relative to the high-temperature cation exchange or one-pot, hot-injection methods. Furthermore, the prevention of self-annealing provides an additional advantage of post-synthetic room temperature cation-doping techniques over the high-temperature routes.[39,40] A room temperature Mn doping of $CsPbCl_3$ QDs using a post-synthetic cation-exchange reaction of $CsPbCl_3$ QDs with $MnCl_2$ was developed by Chen et al.[25] The Mn-doping process was explained with a proposed simultaneous dynamic cation and halogen anion exchange mechanism. The superior performance of $MnCl_2$ compared with other Mn sources for doping Pb halide PQDs might be attributed to the relatively similar bond dissociation energy of Mn-Cl and Pb-Cl bonds, which triggers the successful substitution of Pb with Mn.[25,31,41] Recently, Hills-Kimball et al. demonstrated a quasi-solid-solid cation-exchange route for the synthesis of Mn-doped $CsPbCl_3$ QDs, and proposed a heterogeneous surface doping followed by an inward diffusion process through engineering of the present surface ligands.[42]

The metal cation-doping reactions of Pb halide PQDs are currently studied using conventional, time- and material-intensive flask-based strategies.[25,26,38,39,41] Despite the ease of setup assembly, the batch synthesis approach suffers from major

[1]Department of Chemical and Biomolecular Engineering, North Carolina State University, Raleigh, NC 27695, USA

[2]Department of Chemistry, Brown University, Providence, RI 02912, USA

[3]These authors contributed equally

[4]Lead contact

*Correspondence: abolhasani@ncsu.edu

https://doi.org/10.1016/j.matt.2021.04.025

Please cite this article in press as: Bateni et al., Ultrafast cation doping of perovskite quantum dots in flow, Matter (2021), https://doi.org/10.1016/j.matt.2021.04.025

limitations, including inaccessible *in situ* characterization for fast reactions, batch-to-batch variability, and poor/irreproducible mass transfer rates.[43–46] Such mass transfer limitations can result in non-uniform cation doping of pristine Pb halide PQDs during the fast cation-doping reaction and hinder the accurate systematic and mechanistic studies of interactions between the dopants and host PQDs. Lack of fast homogeneous mixing and *in situ* diagnostic probes in flask-based synthetic routes, make it extremely challenging to accurately study the important dynamics of the fast Mn-doping process under the reaction-limited regime.

Solution-phase synthesis of Mn-doped $CsPbCl_3$ QDs at room temperature are amenable to flow synthesis techniques for accelerated fundamental and applied studies of the PQD-doping process.[47–62] In contrast to batch synthesis techniques, flow synthesis and processing of Pb halide PQDs can provide time- and material-efficient parameter space mapping, enhanced and controllable transport rates for fast reactions, and the prospect of real-time formulation optimization within the broad PQDs synthesis and processing parameter spaces.[43–45] These advantages make in-flow material synthesis an effective strategy for both accurate mechanistic investigations of the doping process and scalable continuous nanomanufacturing of metal cation-doped Pb halide PQDs. Microfluidic flow synthesis techniques can be divided into two primary flow formats, single- and multi-phase flow.[43–45,63] The slow axial/radial diffusive mixing in a single-phase flow regime can result in undesirable axial dispersions, which limit accurate kinetic studies of fast reactions.[43–45] In contrast, the multi-phase flow format benefits from intensified in-flow mixing, due to the formation of axisymmetric recirculation patterns within moving droplets.[43–45] Two-phase (liquid-liquid or gas-liquid) and three-phase (gas-liquid-liquid) flow are two common flow formats utilized for the controlled in-flow nanomaterial synthesis.

The fast kinetics of the solution-phase metal cation-doping reactions of PQDs requires a precisely engineered time-to-space transformation along the length of the flow reactor to acquire *in situ* spectral data with the time resolution needed for the precise dynamic visualization of the cation-exchange reaction. Therefore, it is essential to establish a stable high-flowrate operational envelope, while achieving a uniform mixing pattern within the moving droplets of the multi-phase flow. Despite the enhanced mixing of the reactive phase along the flow direction, the accessible operational window by a two-phase flow format is limited to maintain a stable flow pattern at high fluid velocities.[64,65] However, introduction of an inert gas phase to establish a three-phase flow (gas-liquid-liquid) configuration can significantly expand the operational flow velocity of the uniform multi-phase flow format, leading to simultaneous intensified mixing and the required time resolution for mechanistic studies of mass transfer-limited reactions.[64,65]

In this study, we introduce, *for the first time*, a continuous flow synthetic route for facile Mn doping of $CsPbCl_3$ QDs with a high degree of tunability. We utilize a modular microfluidic platform, shown in Figure 1, for accurate reaction-limited kinetic studies, accelerated mechanistic investigation, and precise emission tuning of Mn-doped $CsPbCl_3$ QDs (Figure 1A) through an in-flow cation-exchange reaction. Next, utilizing the computer-controlled flow synthesis platform equipped with a multimodal *in situ* spectral characterization probe, we systematically investigate the effect of $MnCl_2$ concentration and ligand composition on the kinetics and extent of the room temperature Pb halide PQD cation-doping process. In light of these findings, we propose a heterogeneous surface-doping mechanism mediated by a vacancy-assisted cation migration pathway. This study provides an in-depth

Please cite this article in press as: Bateni et al., Ultrafast cation doping of perovskite quantum dots in flow, Matter (2021), https://doi.org/10.1016/j.matt.2021.04.025

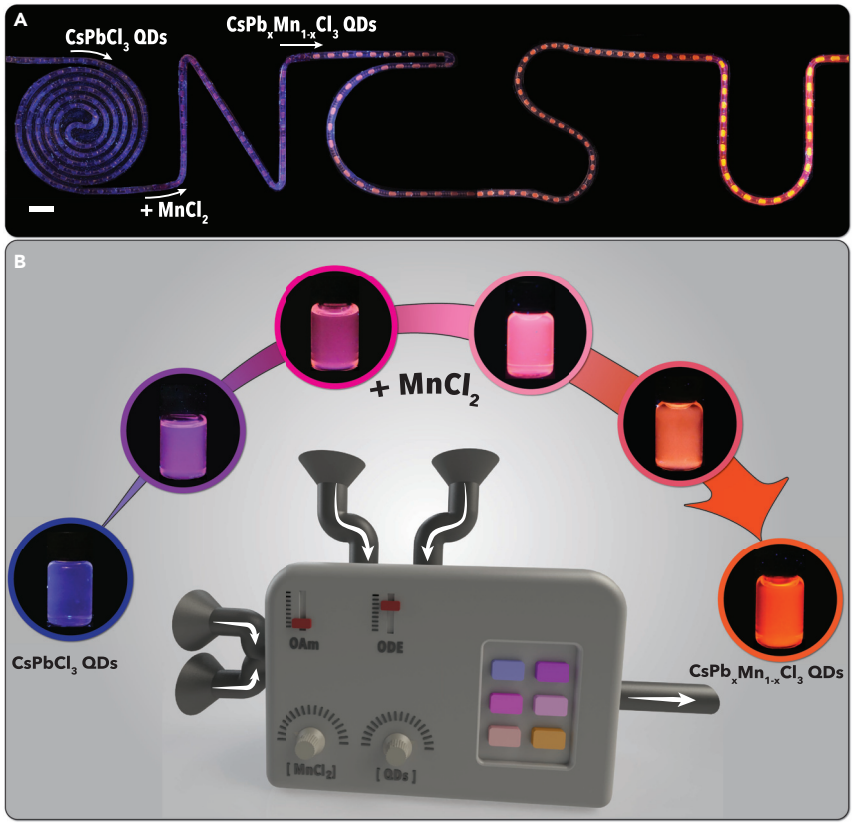

Figure 1. Facile cation doping of $CsPbCl_3$ QDs in flow

(A) Precise tuning of the metal cation doping of $CsPbCl_3$ QDs in flow under UV irradiation (365 nm). Scale bar, 9 mm.

(B) Schematic illustration of the capabilities of the modular microfluidic platform for rapid parameter space exploration, mechanistic studies, and continuous nanomanufacturing of Mn-doped $CsPbCl_3$ QDs.

fundamental understanding of the cation-doping mechanism involved with the surface chemistry of the host Pb halide PQDs and can open new synthetic routes for continuous nanomanufacturing of high-quality cation-doped Pb halide PQDs (Figure 1B) for direct utilization in photonic and optoelectronic devices.

RESULTS AND DISCUSSION

Cation doping in flow

We developed and utilized a computer-controlled modular microfluidic platform to study the post-synthetic metal cation doping of Pb halide PQDs toward enabling continuous on-demand tuning of their optical and optoelectronic properties (Figure 2A). We adapted a single-solvent chemistry to continuously synthesize Mn-doped $CsPbCl_3$ QDs in flow at room temperature (Figure 2B). The choice of a non-coordinating solvent, octadecene (ODE), as the doping solvent was to facilitate continuous nanomanufacturing of cation-doped Pb halide PQDs in the same solvent utilized for the synthesis of the pristine PQDs. Oleylamine (OAm) was used to completely dissolve and activate the dopant source ($MnCl_2$) in the nonpolar reaction solvent (ODE).[42] For the synthesis of the pristine $CsPbCl_3$ QDs, we adapted a modified hot-injection synthesis technique.[42] The PQDs were purified using a conventional precipitation/redispersion strategy. Methyl acetate (MA) was used as a polar

Please cite this article in press as: Bateni et al., Ultrafast cation doping of perovskite quantum dots in flow, Matter (2021), https://doi.org/10.1016/j.matt.2021.04.025

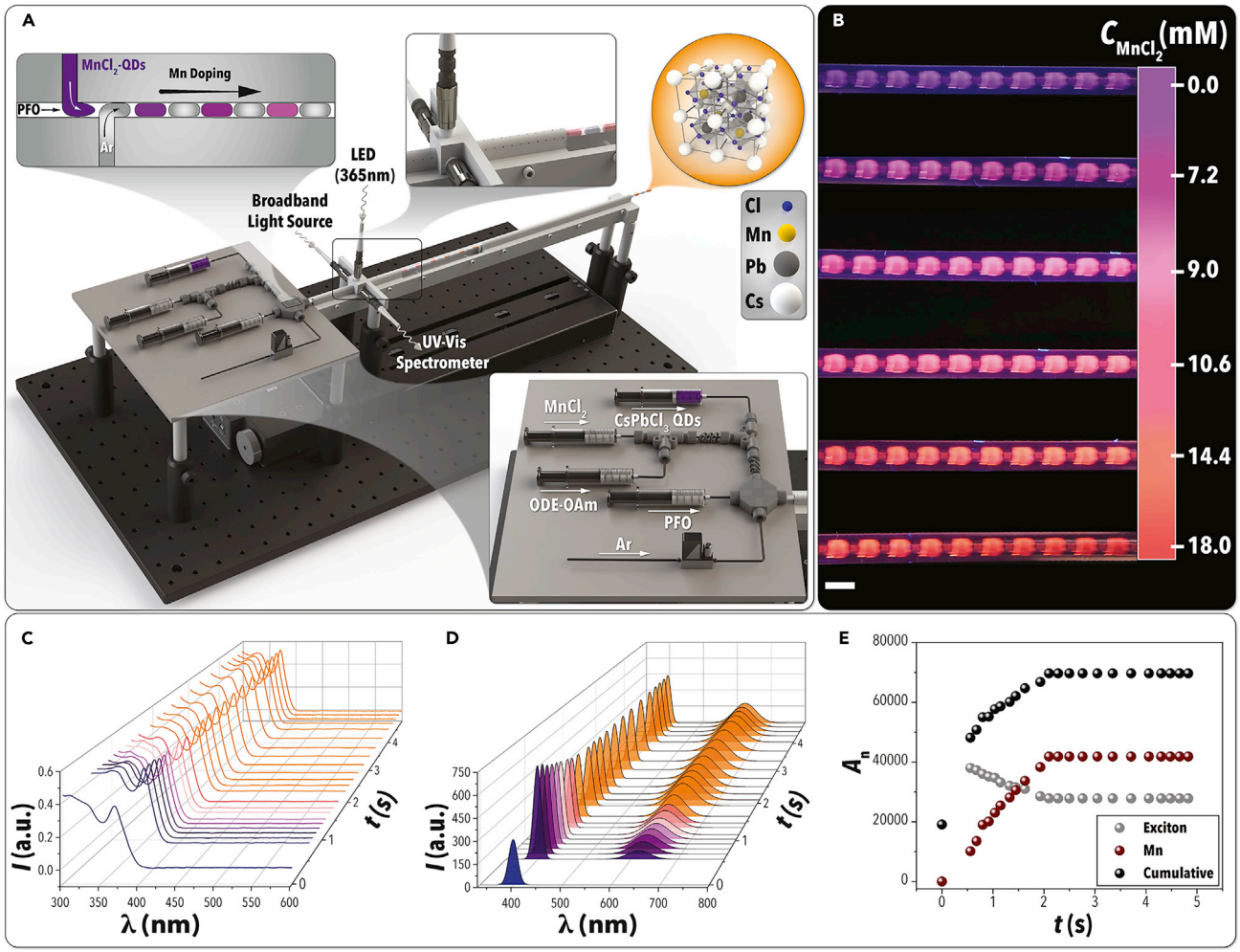

Figure 2. The overall capacity of the automated modular microfluidic platform for the accelerated high-throughput fundamental studies of the room temperature, post-synthetic Mn doping of $CsPbCl_3$ QDs

(A) Schematic illustration of the assembled modular microfluidic platform equipped with a precursor formulation, flow synthesis, and translational flow cell module for ultrafast continuous nanomanufacturing of Mn-doped $CsPbCl_3$ QDs using a three-phase flow format.

(B–D) (B) Fluorescence images of the moving droplets of the Mn-doped $CsPbCl_3$ QDs under UV illumination (365 nm) obtained via an in-flow dilution strategy. Scale bar, 9 mm. A representative 3D waterfall time evolution of the UV-vis (C) absorption and (D) PL spectra of the Mn-doped $CsPbCl_3$ QDs, obtained by the multimodal mobile flow cell.

(E) The normalized exciton and Mn emission peaks and the cumulative area within the room temperature, post-synthetic Mn-doping process.

anti-solvent for the washing step. The pristine $CsPbCl_3$ QDs were diluted to adjust the initial concentration of the Pb halide PQDs for the continuous flow Mn-doping process based on the reported molar extinction coefficient (ϵ).[66,67]

The modular microfluidic platform was integrated with a mobile multimodal spectral characterization probe (UV-vis absorption and PL spectroscopy), capable of monitoring the metal cation-doping process along a 30 cm length of the flow reactor. Two inline static micromixers with a low dead volume (2 μL) were used to ensure homogeneous mixing of the reactive precursors in the formulation module of the microfluidic platform (Figure 2A) before flow segmentation at the custom-built four-way fluidic junction. The addition of advective mixing in a secondary dimension (i.e., Dean flow) induced by the inline braided micromixers enables a fast precursor

Please cite this article in press as: Bateni et al., Ultrafast cation doping of perovskite quantum dots in flow, Matter (2021), https://doi.org/10.1016/j.matt.2021.04.025

mixing timescale, resulting in the reaction-limited Mn-doping process within the moving droplets along the flow reactor.[47] The combination of the built-in micromixers and high flow velocity three-phase flow format allows the in-flow metal cation doping to be operated under the reaction-limited regime, and thereby deconvolutes the effect of precursor mixing rate on the dynamics of the cation-doping process along the 30 cm length of the flow reactor (i.e., reaction times spanning from 0.5 to 5 s with time resolutions as low as 60 ms).[47,48,62] The mobile flow cell provides a broad range of information about the metal cation-doping reaction through temporal *in situ* UV-vis absorption and PL spectroscopy—as the reactive phase droplets move along the flow reactor—including the population of QDs (absorption), the status of PQD surface defects (PL), the colloidal stability of the PQDs (absorption), and the intrinsic kinetics and extent of the cation-doping reaction (PL). Such information would provide valuable insights into the fundamental mechanisms controlling the cation doping of the $CsPbCl_3$ QDs. Figures 2C–2E illustrate an example of the wealth of information about the cation doping of Pb halide PQDs that could be readily obtained using the mobile flow cell integrated with the modular flow reactor.

Figure 2C presents an exemplary time evolution of the UV-vis absorption spectra of Mn-doped $CsPbCl_3$ QDs over 5 s of the post-synthetic cation-doping process. At t = 0 s, the first excitonic peak is located at 375 nm (i.e., the pristine $CsPbCl_3$ QDs). The position of the first excitonic peak wavelength remained constant throughout the metal cation-doping process. However, the second excitonic peak of the absorption spectra became more distinct and the absorption intensity at the first excitonic peak increased and reached a constant value after 2 s of the Mn-doping reaction. These phenomena can be attributed to the suppression of the crystallographic defects (i.e., chloride vacancies and/or distorted $[PbCl_6]^{4-}$ octahedra) presented in the crystalline lattice of the host $CsPbCl_3$ QDs.[68] In addition to the absorption spectra, temporal PL spectra of the PQDs with an excitation wavelength of 365 nm (fiber-coupled LED) were obtained *in situ*, along the flow reactor (Figure 2D). At t = 0 s, the exciton emission peak of the pristine $CsPbCl_3$ QDs is centered at 400 nm with a full-width at half-maximum (FWHM) of 16 nm. At t = 0.56 s, a second emission peak became apparent near 616 nm, which is due to the emergence of radiative recombination pathways through the exciton energy transfer to the Mn internal d states.[30,31] Upon initiation of the metal cation-doping reaction in flow, the intensity of the exciton emission peak increased significantly until t = 0.56 s, which can be attributed to the reduction of non-radiative localized trap states in the pristine $CsPbCl_3$ QDs originating from the surface healing effect of the Mn-doping process.[68] After t = 0.56 s, the exciton peak intensity decreased and the Mn emission peak intensity increased gradually until reaching a plateau at t = 1.63 s, indicating the completion of the Mn-doping reaction. This result shows, *for the first time*, that facile post-synthetic Mn doping of Pb halide PQDs can be achieved at timescales below 2 s. Over the course of the metal-cation doping process, the location and FWHM of the exciton peak remained unchanged, which indicates that the size distribution of the QDs before and after the doping process should be consistent. Moreover, through the cation-doping process, the Mn emission peak red-shifted from 616 to 625 nm ($0.56\ s < t < 1.63\ s$), which is attributed to the formation and enhancement of Mn^{2+}-Mn^{2+} pairs.[33,37,42]

The incorporation of Mn^{2+} ions within the crystalline lattice of the pristine $CsPbCl_3$ QDs is further confirmed through *ex situ* X-band electron paramagnetic resonance (EPR) spectra of the pristine and Mn-doped $CsPbCl_3$ QDs, as shown in Figure S1. Upon doping, the EPR spectra of the Mn-doped $CsPbCl_3$ QDs (Figure S1B) exhibits a single peak with a width of 23.5 G, confirming the successful in-flow doping and

Please cite this article in press as: Bateni et al., Ultrafast cation doping of perovskite quantum dots in flow, Matter (2021), https://doi.org/10.1016/j.matt.2021.04.025

CellPress

incorporation of Mn^{2+} ions into the lattice of the host PQDs through the post-synthetic cation-doping process.[30,37,42] In the case of homogeneous Mn doping, six equally spaced hyperfine profile splitting peaks (A~86 G) are expected in the EPR spectra of the Mn-doped $CsPbCl_3$ QDs.[30,37,42,69] Considering the low amount of the doped Mn in the host $CsPbCl_3$ QDs (1.0% $\pm$ 0.1% Mn^{2+}, measured by energy dispersive X-ray spectroscopy (EDS) elemental mapping), the absence of six hyperfine splitting profiles in the EPR spectra of the Mn-doped $CsPbCl_3$ QDs indicates a strong interaction between the Mn^{2+}-Mn^{2+} pairs localized at the outer surface of the host PQDs. Interestingly, the EPR spectra of the aged Mn-doped $CsPbCl_3$ QDs showed a six-hyperfine splitting profile with a width of 86 G (Figure S1C), which suggests the initiation of the inward diffusion of the surface Mn^{2+} centers into the bulk nanocrystal. This observation can be further confirmed with the slow blue-shift of the Mn emission peak from 625 to 618 nm (Figure S1D) within 6 h after the in-flow Mn-doping process. A similar phenomenon was reported by Hills-Kimball et al. as a result of the homogeneous diffusion of the metal cation dopants into the bulk nanocrystal. From these results, it can be concluded that the in-flow Mn doping of $CsPbCl_3$ QDs is an ultrafast heterogeneous surface-doping reaction (~2 s) followed by a slow inward diffusion process into the bulk nanocrystal (homogeneous).[42]

In addition to the temporal PL and absorption spectra shown in Figures 2C and 2D, the area (A_n) of the exciton and the Mn emission peaks and their cumulative area, normalized with the absorbance value at the excitation wavelength (365 nm) at each instant of time during the metal cation-doping process were measured and presented in Figure 2E. The gradual decrease and increase of the exciton and Mn emission peak intensities (Figure 2D), respectively, imply the direction of the cation-exchange process for the substitution of Pb^{2+} with Mn^{2+} in the PQD surface unit cells. The fact that the Mn-doping process reached completion after only 2 s indicates that the post-synthetic cation-exchange process at room temperature is a fast surface reaction and that the doping process halts once the available Pb^{2+} cations for exchange with Mn^{2+} cations at the outer surface of the PQDs are consumed.[26,38] Figure S2 exhibits the X-ray diffraction (XRD) patterns of the washed pristine $CsPbCl_3$ QDs and the Mn-doped $CsPbCl_3$ QDs. The XRD pattern reveals that both the undoped and doped PQDs are highly crystalline and possess a cubic perovskite $CsPbCl_3$ crystal structure (JCPDS no. 75-0411).[42] There is no noticeable shift in the XRD peak positions before and after the metal cation-doping process and the XRD patterns for the Mn-doped $CsPbCl_3$ QDs remained structurally identical to the washed $CsPbCl_3$ QDs. Previous reports of the homogeneous Mn doping of Pb halide PQDs observed a forward shift in the XRD peak positions after the Mn-doping process as a result of the nanocrystal lattice contraction, since Mn^{2+} ions possess smaller ionic radius than Pb^{2+} ions.[31,37,69,70] Our XRD results are in line with the study of Hills-Kimball et al.,[42] and indicate that the ultrafast post-synthetic Mn-doping process results in an extrinsic surface-doping mechanism, which has no significant effect on the intrinsic regions of the host PQDs and is not involved with an inward diffusion process toward the core structure of PQDs during the in-flow cation-doping reaction (~2 s). Transmission electron microscopy (TEM) images of the pristine $CsPbCl_3$ and Mn-doped $CsPbCl_3$ nanocubes are shown in Figure S3. TEM images of the pristine and Mn-doped $CsPbCl_3$ QDs show a uniform cubic morphology. The preservation of the average cube length of the PQDs before and after the post-synthetic metal cation-doping process further confirms the heterogeneous surface-doping mechanism.

To have a deeper look into the heterogeneous surface-doping mechanism of the Mn-doped Pb halide PQDs, we need to first build an understanding of the surface

Please cite this article in press as: Bateni et al., Ultrafast cation doping of perovskite quantum dots in flow, Matter (2021), https://doi.org/10.1016/j.matt.2021.04.025

chemistry of the starting $CsPbCl_3$ QDs. It has been demonstrated that isolation and purification of Pb halide PQDs using polar solvents besides further dilution steps may deteriorate their colloidal/structural integrity because of the detachment of surface capping ligands, and thus the formation of surface defects, including chloride vacancies and distorted $[PbCl_6]^{4-}$ octahedra.[71,72] Thus, the post-synthetic Mn-doping process can prevent the energy transfer loss through the pre-existing surface defects by filling the chloride vacancies, completing the distorted surface unit cells of the pristine Pb halide PQDs, and forming a protective shell around the outer surface of the host PQDs. The time evolution of the peak emission areas during the Mn doping of Pb halide PQDs (Figure 2E) reveals that the cumulative area increases until 2 s of the metal cation-exchange reaction and then reaches a plateau, which indicates the successful removal of some of the surface defects present at the surface of the pristine PQDs, which was further confirmed through increased total PLQY of the QDs from 0.5% (pristine $CsPbCl_3$ QDs) to 4% (Mn-doped $CsPbCl_3$ QDs). Furthermore, the constant values of the exciton and Mn emission peaks areas after 2 s provide additional evidence for the completion of the ultrafast in-flow cation-exchange reaction through a heterogeneous surface-doping mechanism. It should be noted that, although there are significant mass transfer and reaction kinetics limitations in batch reactors, which affect the accurate kinetic studies of the ultrafast metal cation-doping reaction in a batch reactor, we do not expect a significant difference in the final PLQY of the Mn-doped $CsPbCl_3$ QDs obtained by the flow versus batch reactors; PLQY of the Mn-doped $CsPbCl_3$ QDs synthesized in batch was 3.5%.

Mechanistic studies in flow

To better understand the mechanism of the metal cation doping of Pb halide PQDs, in the next set of experiments, we used the modular microfluidic platform to investigate the effects of the dopant concentration and the ligand composition on the kinetics and extent of the post-synthetic cation-exchange reactions. The chemistry of the Mn precursor used in this study includes an activated Mn precursor (i.e., a $MnCl_2$-OAm complex), as well as free chloride (Cl^-) and oleylammonium (OAm^+) ions that play important roles during the surface-doping reaction. A systematic in-flow study of the effects of $MnCl_2$ concentration (C_M) and the ligand-to-solvent ratio ($L_{RS} = V_{OAm}/V_{ODE}$; where V_{OAm} is the volume of OAm and V_{ODE} is the volume of ODE) on the kinetics and extent of the metal cation doping provides the synthesis science knowledge and framework to enable precision synthesis and fine-tuning of the optical and optoelectronic properties of Pb halide PQDs through a continuous, post-synthetic Mn-doping process.

Effect of $MnCl_2$ concentration on the in-flow cation doping

To study the effect of cation dopant concentration on the kinetics and extent of Pb halide PQD doping, we utilized the in-flow dilution module of the microfluidic synthesis platform to rapidly adjust the concentration of the dopant precursor before mixing with the host PQDs in the flow reactor. A concentrated stream of the $MnCl_2$ precursor was mixed with a stream of the dilution solution containing the same solvent (ODE) and L_{RS}. Different concentrations of $MnCl_2$ were obtained by changing the volumetric flowrates of both fluidic streams, while keeping the total volumetric flowrate constant. As shown in Figure 2B, it was observed that the emission color of the Mn-doped $CsPbCl_3$ QDs could be tuned from blue-violet to orange by continuously varying the concertation of the reactive $MnCl_2$ precursor on the fly. For the purpose of our mechanistic studies, we monitored the metal cation doping of $CsPbCl_3$ QDs with six different concentrations of the dopant precursor. Figure 3A (and Figure S4A) presents the steady-state UV-vis absorption spectra of the pristine and the Mn-doped $CsPbCl_3$ QDs. As can be seen in Figure 3A, the intensity of the

Please cite this article in press as: Bateni et al., Ultrafast cation doping of perovskite quantum dots in flow, Matter (2021), https://doi.org/10.1016/j.matt.2021.04.025

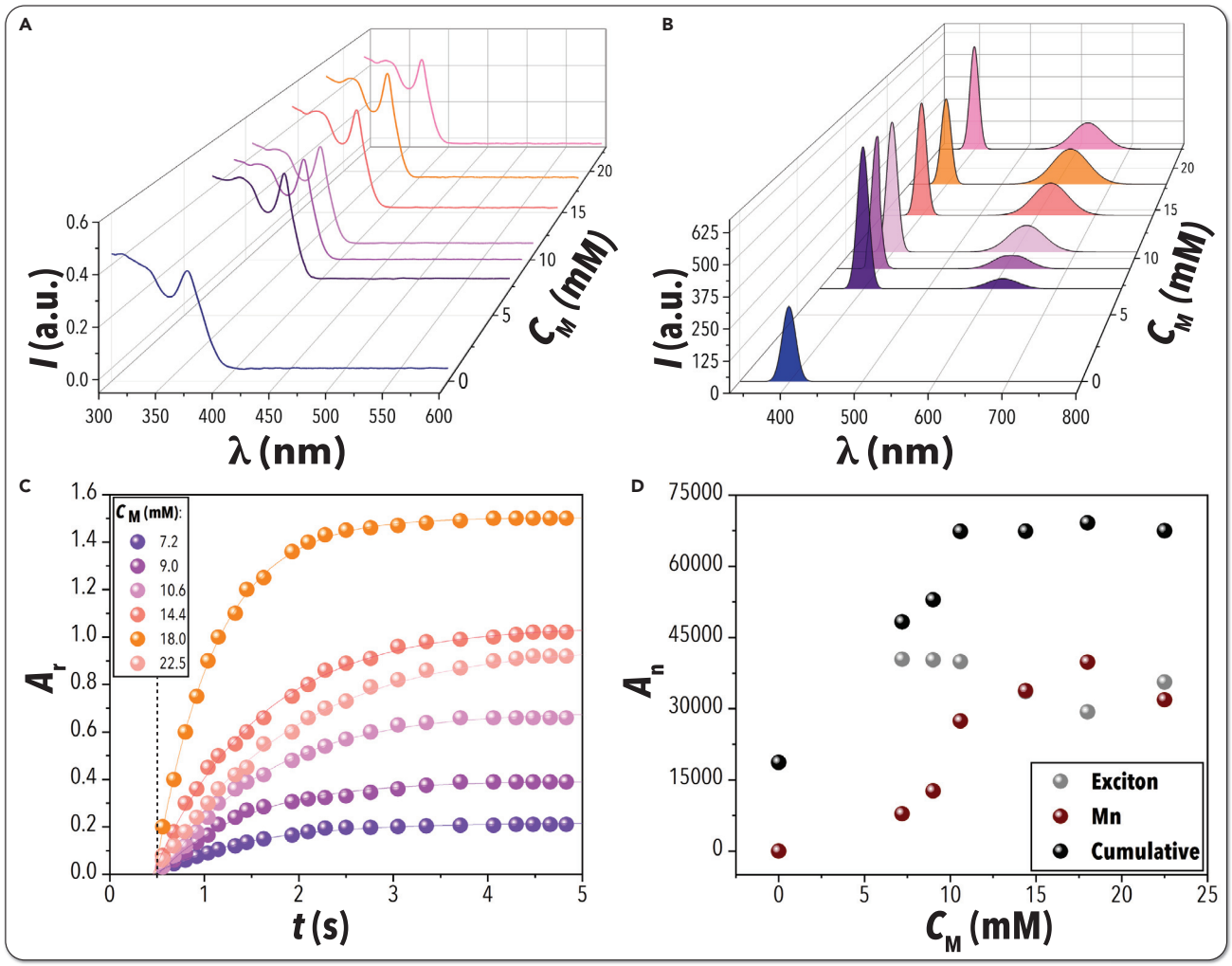

Figure 3. Effect of the metal cation dopant concentration (C_M) on the kinetics and extent of the in-flow doping process

(A and B) The steady-state UV-vis (A) absorption, and (B) PL spectra of the pristine and Mn-doped $CsPbCl_3$ QDs at different concentrations of the dopant precursor.

(C) The area ratio (A_r) variation of the exciton to Mn emission peaks over the course of the in-flow metal cation-doping process for different C_M values. The first 0.5 s is considered as the incubation time of the heterogeneous surface-doping mechanism.

(D) The normalized exciton, Mn, and total emission peaks of the Mn-doped $CsPbCl_3$ QDs at different C_M values.

first excitonic peak increased after doping, while its peak wavelength remained unchanged. This observation confirms the effect of the metal cation doping in removal of some of the surface defects present in the pristine PQDs through a heterogeneous surface-doping approach.[68] The steady-state PL spectra of Mn-doped $CsPbCl_3$ QDs with different $MnCl_2$ concentrations, shown in Figure 3B (and in Figure S4B), revealed that the exciton peak intensity was enhanced drastically by the metal cation doping and then decreased, while the Mn emission peak increased until a certain C_M value (18 mM), thereby suggesting a two-stage cation-doping process: (1) defect removal and surface treatment of the pristine Pb halide PQDs and (2) initiation of the room temperature metal cation exchange with surface Pb^{2+} cations. When changing C_M from 7.2 to 18 mM, the exciton peak wavelength and FWHM of the Mn-doped $CsPbCl_3$ QDs remained unchanged. However, the Mn emission peak red-shifted from 616 to 625 nm, accompanied by an increase in its area, indicating

Please cite this article in press as: Bateni et al., Ultrafast cation doping of perovskite quantum dots in flow, Matter (2021), https://doi.org/10.1016/j.matt.2021.04.025

a higher extent of Mn doping within the host $CsPbCl_3$ QDs at higher C_M values. Interestingly, when increasing the C_M value from 18 to 22.5 mM, the exciton peak intensity increased, while the Mn emission peak decreased and blue shifted to 619 nm. This observation suggests that, at very high C_M values, the cation-exchange rate decreases, and the extent of doping reduces, which can be attributed to the diffusion limitations induced by the presence of excess inactivated Mn^{2+} cations inhibiting the exchange of the activated Mn^{2+} cations with the surface Pb^{2+} cations.

To further study the kinetics and the extent of the post-synthetic Mn doping of Pb halide PQDs, we introduced the term area ratio (A_r), which is defined as the ratio of the area under the Mn emission peak to the area under the exciton peak. Figure 3C shows how A_r varies during the metal cation-exchange reaction in flow for six different dopant concentrations. Figure 3C reveals important information about the mechanism as well as the kinetics and extent of the metal cation-doping process. One of the most important results of our study is that, regardless of the operating C_M value, the first Mn emission peak only appears after ~0.5 s of the reaction time. This delay in the appearance of the Mn emission peak is referred as the *incubation time* in our study. Upon injection of the dopant precursor into the stream of the pristine $CsPbCl_3$ QDs, the excess Cl^- anions rapidly fill the Cl^- vacancies present at the surface of the pristine $CsPbCl_3$ QDs, and thus significantly reduces the population of the available distorted unit cells.[26,71,72] During the incubation time, the excess free OAm^+ ions bind to the halide sites at the outer surface unit cells, forming an x-type oleylammonium chloride ligand shell.[72] These two processes can explain the healing effect of the Mn-doping reaction for the removal of the surface defects in the beginning of the post-synthetic metal cation-doping process (i.e., the increased exciton peak emission area). Next, the activated dopant precursors (i.e., $MnCl_2$-OAm complex) bind to the available Cl^- anions in the halide sites at the outer surface of the PQDs to initiate the cation-exchange process.[26] As shown in Figure 3C, by increasing the dopant concentration from 7.2 to 18 mM, the extent and intrinsic kinetics of the Mn-doping reaction increased up to C_M = 22.5 mM, and then decreased due to the less available free oleylammonium ions to bind to the surface of the pristine $CsPbCl_3$ QDs and remove surface Pb^{2+} cations for the cation-exchange reaction. The intrinsic kinetic constant (k_1) values of the Mn-doping reaction at different C_M values are presented in Figure S5A, which follow the same trend of A_r discussed previously.

Figure 3D presents the normalized individual and the cumulative area under the exciton and the Mn emission peaks. It is apparent that, during the surface doping of $CsPbCl_3$ QDs, the surface defects of the Pb halide PQDs are reduced, as the total peak emission areas of the Mn-doped $CsPbCl_3$ QDs increased for all tested dopant concentrations. When increasing the dopant concentration, the exciton peak area reduced until C_M = 18 mM and then increased at C_M = 22.5 mM. Likewise, the normalized Mn emission peak area increased until C_M = 18 mM and then decreased at C_M = 22.5 mM. This finding is aligned with our previously proposed surface-doping mechanism. At the maximum Mn doping (C_M = 18 mM), all the available surface Pb^{2+} cations are exchanged with the activated dopant precursor.[26,38] At C_M = 22.5 mM, as the amount of OAm in the dopant precursor is constant, higher amounts of free Mn^{2+} cations are available in the dopant stream. The presence of free Mn^{2+} cations can interrupt the transfer of the activated $MnCl_2$-OAm complexes and inhibit their attachment to the halide sites and, as a result, fewer numbers of Pb^{2+} and Mn^{2+} cations can be exchanged at the surface of the $CsPbCl_3$ QDs.

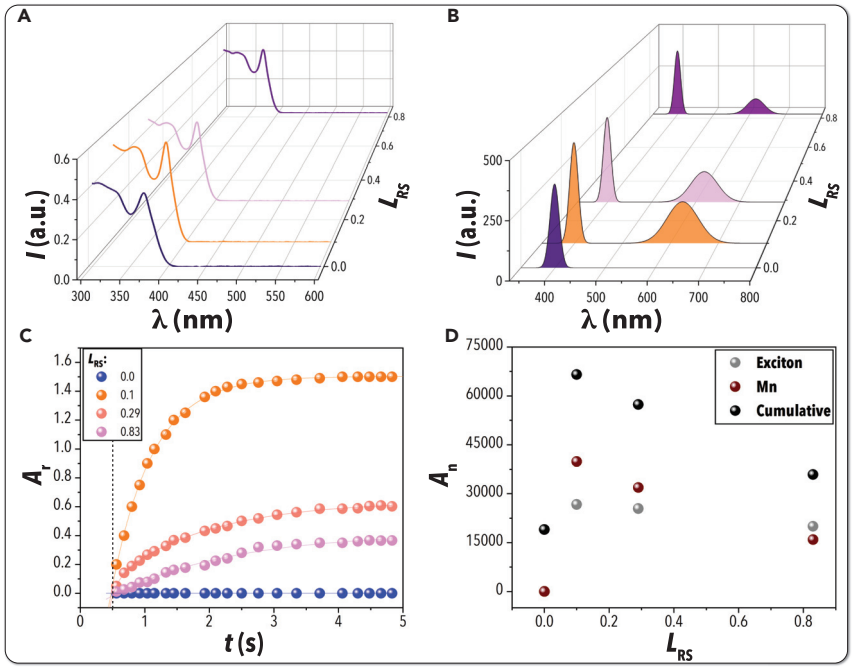

Figure 4. Effect of ligand-to-solvent ratio (L_{RS}) on the kinetics and extent of the in-flow Mn-doping process

(A and B) The steady-state UV-vis (A) absorption and (B) PL spectra of the pristine and Mn-doped $CsPbCl_3$ QDs at different ligand-to-solvent ratios.

(C) The area ratio (A_r) variation of the exciton to Mn emission peaks over the course of the in-flow metal cation-doping process for different L_{RS} values. The first 0.5 s is considered as the incubation time of the heterogeneous surface-doping mechanism.

(D) The normalized exciton, Mn, and total emission peaks of the Mn-doped $CsPbCl_3$ QDs at different L_{RS} values.

Effect of ligand-to-solvent ratio on the in-flow cation doping

Following the studies of the effect of dopant concentration on the cation doping of Pb halide PQDs, in the next set of experiments we assessed the effect of ligand composition present in the dopant precursor on the heterogeneous surface-doping reaction. The concentration of the $MnCl_2$ salt remained constant while varying the ligand-to-solvent ratio. Four different L_{RS} values were explored for our in-flow cation-doping studies. Figure 4A (and Figure S4C) shows the steady-state UV-vis absorption spectra of the Mn-doped $CsPbCl_3$ QDs at different L_{RS} values. Except for $L_{RS} = 0$, the absorption intensity at the first excitonic peak increased after Mn doping, which confirms the role of the cation doping in the elimination of the localized surface traps. It should be noted that, at $L_{RS} = 0$ (i.e., in the absence of OAm), the $MnCl_2$ salt cannot be completely dissolved in ODE.[42] Therefore, the absence of surface-doping reaction is expected at $L_{RS} = 0$. The steady-state PL spectra of the four studied ligand compositions are shown in Figure 4B (and Figure S4D). At $L_{RS} = 0$, there is no evidence of the Mn emission peak, indicating the lack of Mn doping in the absence of OAm to activate the doping precursor. The critical role of the OAm for the activation of the $MnCl_2$ precursor and the Mn-doping surface reaction has previously been demonstrated.[26,42] We postulated that the formation of the activated $MnCl_2$-OAm complexes in the dopant precursor, followed by their binding to the halide sites in the truncated $[PbCl_6]^{4-}$ octahedra present at the outer surface of the pristine $CsPbCl_3$ QDs, provides an opportunity for the $MnCl_2$-OAm complexes to be exchanged with $PbCl_2$-OAm at the surface octahedra through a cation

Please cite this article in press as: Bateni et al., Ultrafast cation doping of perovskite quantum dots in flow, Matter (2021), https://doi.org/10.1016/j.matt.2021.04.025

migration. At L_{RS} = 0.1, as a result of surface-doping reaction, the exciton peak intensity increased and the Mn emission peak became apparent. However, by further increasing the L_{RS} beyond 0.1, the exciton and Mn emission peaks both diminished. A similar trend was observed in the A_r values (Figure 4C) and the intrinsic doping constant (Figure S5B), indicating a slower intrinsic kinetic and lower extent of the Mn doping at high L_{RS} values. This phenomena could be attributed to the fact that, at higher L_{RS} values, higher amounts of free OAm^+ ions might deteriorate the host $CsPbCl_3$ QDs.[42] Therefore, at high L_{RS} values, lower amounts of octahedra, and thus the surface Pb^{2+} cations are available to be exchanged with the activated dopant precursors. Moreover, due to the higher availability of excess OAm^+ ions at high L_{RS} values, similar to the effect of high C_M values, fewer $MnCl_2$-OAm complexes could be exchanged at the surface of the pristine $CsPbCl_3$ QDs, due to the induced diffusion limitations. These observations are in line with the observation of the exciton and Mn emission peak areas at different L_{RS} values, as shown in Figure 4D. At L_{RS} > 0.1, the normalized exciton and Mn emission peak areas, as well as the total emission peak areas, decreased for all L_{RS} values tested here, which indicates a lower extent of Mn doping as a result of the lower cation-exchange reaction rates. The decrease in both the normalized Mn emission peak area and the normalized exciton peak area suggests (1) lower amounts of surface Pb^{2+} cations present at high L_{RS} values and (2) a lower exchange rate between the $MnCl_2$-OAm complexes and $PbCl_2$-OAm units at the surface unit cells. Furthermore, we studied the detrimental effect of high amounts of free OAm^+ ions on the colloidal integrity of the PQDs and the dynamics of the cation-doping process. Figures S6A and S6B show the *in-situ*-obtained UV-vis absorption spectra of the pristine $CsPbCl_3$ QDs diluted in flow with ODE in the absence and presence of OAm (L_{RS} = 0.1), respectively. As shown in Figures S6A and S6B, the absorption intensity values diminished slightly in the presence of OAm and reached a plateau within 2 s. Moreover, the effect of OAm on the UV-vis absorption spectra of the washed $CsPbCl_3$ QDs at different dilution ratios were studied and are presented in Figure S6C. As expected, in the presence of high concentration of OAm, the well-defined excitonic features of the UV-vis absorption spectra of $CsPbCl_3$ QDs were diminished, indicating the degradation of $CsPbCl_3$ QDs. Therefore, it can be concluded that, at high L_{RS}, both the structural integrity of the $CsPbCl_3$ QDs and the kinetics and the extent of the Mn-doping reaction could be negatively impacted.

In summary, the automated modular microfluidic platform enabled us to reveal the complex dynamics of the heterogeneous surface cation doping of Pb halide PQDs that was otherwise impossible to deconvolute and study using conventional flask-based synthesis techniques. Moreover, the developed modular microfluidic platform in this work can be readily adapted for accurate fundamental investigations and continuous flow doping of other nanocrystals hosts and impurities. In one example, we utilized the same flow chemistry strategy developed in this work to perform successful Mn doping of $CsPbBr_3$ QDs—synthesized using our previously reported protocol.[47] Figure S7 shows the steady-state UV-vis absorption and PL spectra of the pristine and Mn-doped $CsPbBr_3$ QDs. As shown in Figure S7, upon Mn doping of $CsPbBr_3$ QDs, the excitonic PL peak blue shifted from 492 to 408 nm as a result of simultaneous anion exchange and cation-doping reactions.

Based on our *in situ* spectral and offline structural characterization results, we propose a vacancy-assisted cation migration mechanism for the room temperature, post-synthetic Mn doping of $CsPbCl_3$ QDs. Figure 5 shows a schematic illustration of the surface processes involved during the heterogeneous metal cation doping of Pb halide PQDs. This mechanism is dissected into two stages of (1) an early-stage

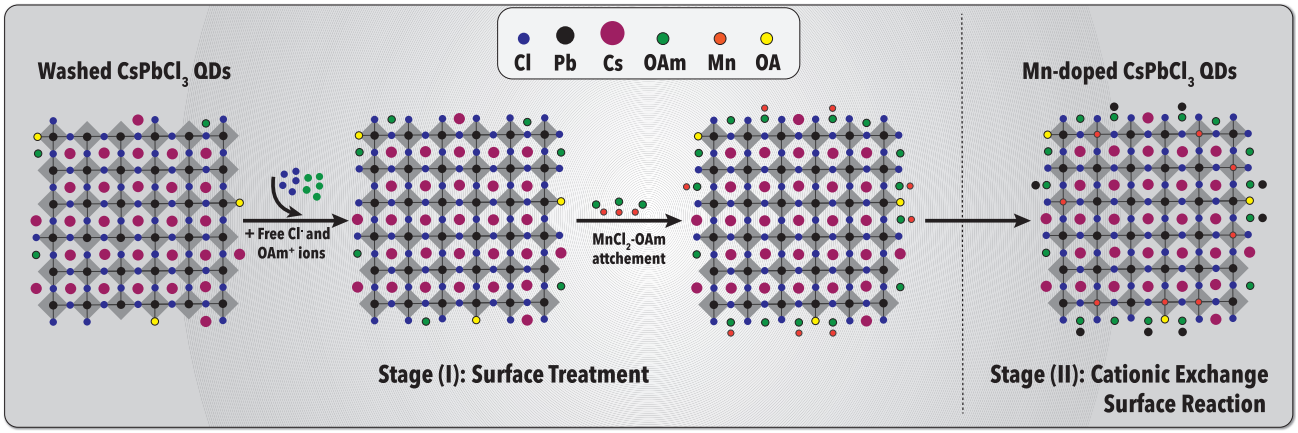

Figure 5. Proposed metal cation-doping mechanism

Schematic illustration of the vacancy-assisted metal cation migration mechanism during the room temperature, post-synthetic Mn doping of $CsPbCl_3$ QDs.

surface healing/treatment reaction within the incubation time (~0.5 s), and (2) a surface cation-exchange reaction that can be rapidly conducted in ~2 s.

Given the labile ionic nature of the ligands and ligand-metal bindings, the purification of the $CsPbCl_3$ QDs with a polar MA anti-solvent and then the following dilution steps, desorb a major fraction of ligands around the surface of the pristine PQDs.[68,71] The surface defects of the washed $CsPbCl_3$ QDs cannot only be limited to the ligand removals and includes the formation of Cl^- vacancies and distorted octahedra unit cells mostly at the outer surface of the PQDs.[71] Upon mixing of the $MnCl_2$ precursor with the purified $CsPbCl_3$ QDs, the excess free Cl^- anions present in the dopant precursor fill the vacant halide sites of truncated $[PbCl_6]^{4-}$ unit cells present at the surface of the PQDs. Next, the excess free unprotonated OAm^+ cations, coming from the $MnCl_2$ precursor, bind to the Cl^- anions located in the surface unit cells and form the x-type oleylammonium chloride ligand shell.[26,72] De Roo et al. has previously demonstrated that the surface of the $CsPbBr_3$ nanocrystals can be passivated through a pair of x-type ligands, binding with the oleylammonium cations to the surface bromide sites.[72] Following these two steps, a portion of localized surface traps are removed, and a new ligand shell environment is created around the outer surface of the $CsPbCl_3$ QDs. The enhanced UV-vis absorption intensity values of the first excitonic peak, along with the enhanced exciton emission peak intensity at the early stage of the metal cation-doping process, further support the existence of a surface defect removal step in the surface-doping mechanism. Then, the activated $MnCl_2$-OAm complexes can attach to the available halide sites in the surface unit cells to initiate the Mn-doping process.[26]

In the second stage of the cation-doping process, the $MnCl_2$-OAm complex is exchanged with the $PbCl_2$-OAm complex in the surface unit cell, forming the surface $[MnCl_6]$ octahedra, passivated by oleylammonium chloride ligands.[26,72] Due to the rigid structure of Pb^{2+} cations surrounded by halide salts, a high activation energy is required to form Pb^{2+} vacancies and perform Pb^{2+}-to-Mn^{2+} cation-exchange reactions.[38,41] When the concentration of $MnCl_2$ increases, the population of the activated $MnCl_2$-OAm complexes increases, and therefore the extent of Mn doping is enhanced and the cation-exchange surface reaction reaches completion in a shorter period of time (i.e., faster intrinsic doping kinetics). However, upon further

Please cite this article in press as: Bateni et al., Ultrafast cation doping of perovskite quantum dots in flow, Matter (2021), https://doi.org/10.1016/j.matt.2021.04.025

increasing the concentration of $MnCl_2$ in the dopant precursor at a constant L_{RS}, the number of available free Mn^{2+} cations in the dopant precursor increases, which disrupts the dynamics of the doping process by inducing mass transfer limitations for the activated $MnCl_2$-OAm complexes. Therefore, the cation-exchange reaction rate and the extent of Mn-doping decrease. In addition, at high ligand-to-solvent ratios ($L_{RS} > 0.1$), the basic environment induced by OAm^+ cations, deteriorates the integrity of the $CsPbCl_3$ QDs present in the reaction mixture. In addition, at high values of L_{RS} (similar to high C_M), excess OAm^+ cations can promote diffusion limitations and decrease the cation-exchange rate. The low activation energy requirement for the formation of Cl^- vacancies enables the $MnCl_2$-OAm complex to be exchanged with the $PbCl_2$-OAm surface unit through the proposed vacancy-assisted cation migration mechanism.[26,38]

Conclusions

In conclusion, we introduced a facile and tunable microfluidic synthesis approach for the continuous metal cation doping of Pb halide PQDs. We utilized a modular robotic flow synthesis platform for the time- and resource-efficient mechanistic investigations of the metal cation doping of $CsPbCl_3$ QDs with a high degree of emission tunability. The integration of a mobile, multimodal spectral characterization probe with the modular microfluidic platform allowed us to accurately study the kinetics and reveal the mechanism of the metal cation doping of $CsPbCl_3$ QDs with a time resolution of 60 ms, which is otherwise impossible using current flask-based QD synthesis strategies. Utilizing the developed microfluidic platform, we rapidly investigated the effect of the metal cation dopant precursor concentration and ligand composition on the optoelectronic properties of Mn-doped $CsPbCl_3$ QDs and proposed a two-stage heterogeneous surface-doping mechanism through the vacancy-assisted metal cation migration.

In addition to the fundamental mechanistic studies of the metal cation-doping process, we demonstrated the first ultrafast continuous nanomanufacturing route (~2 s reaction time) of precision-tailored Mn-doped $CsPbCl_3$ QDs for next-generation energy technologies. Further development and adoption of the developed in-flow metal cation-doping strategy toward other impurity-doped nanomaterials is expected to significantly accelerate development of optimal formulations of novel energy-relevant nanomaterials with unique physicochemical and optoelectronic properties at a fraction of the time and cost of currently utilized batch techniques.

EXPERIMENTAL PROCEDURES

Resource availability

Lead contact

Further information and requests for resources and reagents should be directed to and will be fulfilled by the lead contact, Milad Abolhasani (abolhasani@ncsu.edu).

Materials availability

This study did not generate new unique reagents.

Data and code availability

The in-flow metal cation-doping data are available upon request.

Materials

Lead (II) chloride (99%) and $MnCl_2$ (97%, anhydrous) were purchased from STREM Chemicals. MA (99%, extra pure) and 1-octadecene (ODE) (90%) was purchased from ACROS Organics. Oleylamine (OAm) (70%), oleic acid (OA) (90%), and cesium

Please cite this article in press as: Bateni et al., Ultrafast cation doping of perovskite quantum dots in flow, Matter (2021), https://doi.org/10.1016/j.matt.2021.04.025

carbonate (Cs_2CO_3) (99.9%) were purchased from Sigma-Aldrich. Hexane (certified ACS) was purchased from Fisher Scientific. High-performance heat transfer perfluorinated oil (PFO) (Galden HT 270) was purchased from Solvay. Argon (Ar) and nitrogen (N_2) tanks were purchased from Airgas. All the chemicals were used without further purifications.

Preparation of $CsPbCl_3$ QDs

$CsPbCl_3$ QD precursors were prepared by adapting the procedure reported by Hills-Kimball et al. with slight modifications.[42] First, the Cs-oleate precursor was prepared by loading 102 mg Cs_2CO_3, 5 mL ODE, and 312.5 μL OA in a 24 mL septa vial and heating at 120°C for 1 h under vacuum to obtain a clear solution. To ensure complete dissolution of Cs_2CO_3, the solution remained at 120°C and was heated for 1 h under N_2. The vacuum and the flow of N_2 were controlled using an in-house Schlenk line system. Next, 0.748 mmol $PbCl_2$ (208 mg), 20 mL ODE, 2 mL dried OA, and 2 mL dried OAm were added into a 100 mL 3-neck flask, followed by heating under vacuum at 120°C for 1 h to obtain complete dissolution of $PbCl_2$ salts. Then, the mixture was heated to reach 170°C under N_2 and vigorous stirring. To synthesize $CsPbCl_3$ QDs, 1.6 mL of the Cs-oleate precursor was rapidly injected into the heated $PbCl_2$ solution and the mixture was immediately cooled in an ice bath. To purify the synthesized $CsPbCl_3$ QDs, the crude mixture was washed with MA with a volumetric ratio of 1:2 $CsPbCl_3$ QDs:MA. The collected colloidal suspension was then centrifuged at 6,500 rpm for 6 min to separate the white precipitates of PQDs from the supernatant. The precipitated $CsPbCl_3$ QDs were re-dispersed in ODE to form the colloidally stable washed QDs for the in-flow cation-doping studies. The initial concentration of the $CsPbCl_3$ QDs were maintained at 3.3×10^{-7} M using the absorbance value at 380 nm and reported intrinsic absorption coefficient for the size distribution of $CsPbCl_3$ QDs spanning from 9 to 11 nm.[66,67]

Preparation of the $MnCl_2$ precursor

To prepare the $MnCl_2$ precursor, 0.8 mmol dried $MnCl_2$ (100.6 mg) salts, 20 mL ODE, and 2 mL dried OAm (L_{RS} = 0.1) were loaded in a 40 mL septa vial and heated under flow of N_2 at 120°C for 2 h to completely s dissolve the $MnCl_2$ salt.

In-flow experimentation

Microfluidic platform

Flow synthesis of Mn-doped $CsPbCl_3$ QDs was carried out in an automated modular microfluidic platform previously developed in our group.[47,48] The assembly of the microfluidic platform involves three structural core modules of the support structure, flow cell, and sampling tracks (custom machined in aluminum, Stratasys Direct Manufacturing). All the fluid-streaming components (tubing, fluidic connections, and fittings) were purchased from IDEX-Health & Sciences. An in-house LabVIEW script was utilized to centralize control of different modules of the automated microfluidic platform, including a dual syringe pump (Chemyx, Fusion 4,000), a mass flow controller (Bronkhorst, EL-FLOW Select), a 30 cm translational stage (Thorlabs, LTS300, with a maximum linear velocity of 5 cm s^{-1}), a high-power LED (Thorlabs, M365LP1), fiber-coupled light source (Ocean Insight, DH-2000BAL), and a fiber-coupled photospectrometer (Ocean Insight, Ocean HDX Miniature Spectrometer).

In-flow cation doping of Pb halide PQDs

Continuous metal cation doping of $CsPbCl_3$ QDs was carried out at room temperature in the modular microfluidic platform shown in Figure 2A. The washed $CsPbCl_3$ QDs and $MnCl_2$ precursor were loaded in gas-tight stainless steel (SS) syringes (Chemyx, 50 mL) under inert conditions. To achieve in-flow concentration tuning

Please cite this article in press as: Bateni et al., Ultrafast cation doping of perovskite quantum dots in flow, Matter (2021), https://doi.org/10.1016/j.matt.2021.04.025

of the dopant precursor, the dopant solvent (ODE) with the same ligand-to-solvent ratio (OAm:ODE) was prepared and loaded in another SS syringe under inert conditions. Fluorinated ethylene propylene (FEP) tubing (0.02″ ID, 1/16″ OD) was utilized to connect the precursor syringes to off-the-shelf T-junctions and a custom-designed polyether ether ketone (PEEK) four-way junction. The FEP tubing (0.01″ ID, 1/16″ OD) was also used to fabricate two inline static micromixers with a dead volume of 2 μL for intensifying the microscale mixing efficiency of the chemical precursors.[47,49,55,56] The concentrated $MnCl_2$ precursor and dilution solution streams were directed to an off-the-shelf T-junction and then passed through a braided micromixer to continuously adjust the concentration of the dopant precursor before the cation-doping process. Next, the diluted stream of $MnCl_2$ and washed $CsPbCl_3$ QDs were mixed in another in-series T-junction and braided micromixer to achieve a homogeneous reactive mixture before entering the modular microfluidic reactor. The pre-mixed cation-exchange reaction solution and the inert carrier fluids (i.e., Ar and PFO) were then directed to the modified PEEK cross-junction to form a three-phase flow throughout the flow reactor (FEP tubing, 1/16″ ID, 1/8″ OD). The in-flow cation-doping process was accurately and thoroughly monitored at different residence times along the flow reactor without changing the precursor flowrates (i.e., mixing timescale). The mobile three-port flowcell installed on the translational stage enabled monitoring of the fast cation-doping reaction through time-to-space transformation at 22 distinct optical ports. Concentrations of the dopant precursor and OAm were tuned on the fly by adjusting the volumetric flow rates of the washed $CsPbCl_3$ QDs (Q_1) and the diluted $MnCl_2$ precursor ($Q_2 = Q_{2\text{-}1} + Q_{2\text{-}2}$; where $Q_{2\text{-}1}$ and $Q_{2\text{-}2}$ are the volumetric flow rates of the concentrated $MnCl_2$ precursor and the dilution solution, respectively) to be $Q_1{:}Q_2$ = 1:1. To establish a stable three-phase flow at high axial flow velocity (Video S1) for reaction-limited kinetic and mechanistic studies of the cation-doping process, the flow rates of Ar and PFO streams were set at 5 and 1 mL/min, respectively. Mathematical correction factors were calculated and applied to ensure identical absorption and photoluminescence results for one unique sample across all optical monitoring ports along the flow reactor.[48]

Flow cell validation

A 1 × 10 mm quartz cuvette was used for offline absorption validation of the *in-situ*-obtained spectra via the three-port flow cell installed on the translational stage. Moreover, the accurate PL spectroscopy by the mobile flow cell was validated, using a bench-top PL spectrometer (Edinburgh FS5). As shown in Figure S8, the *in-situ*-obtained absorption and PL spectra from the microfluidic platform matched the spectra obtained from the offline measurements with the quartz cuvette and PL spectrometer.

Offline characterization

The washed $CsPbCl_3$ QDs and Mn-doped $CsPbCl_3$ QDs were analyzed using TEM and XRD. TEM imaging was conducted using an FEI Talos F200X operated at an acceleration voltage of 200 kV to acquire the morphology of the PQDs. TEM samples were prepared by drop-casting the PQD solution onto a copper TEM grid (Ted Pella, 200 Mesh Carbon Film). To characterize the crystalline structure of the in-flow synthesized Mn-doped $CsPbCl_3$ QDs, XRD patterns were recorded using a Rigaku SmartLab X-Ray diffractometer equipped with Cu Kα radiation (λ = 0.154 nm) operating at 40 kV. Supplementary elemental mapping was carried out using the EDS of FEI Talos F200X. EPR spectroscopy measurements were conducted using a Bruker ELEXSYS E500 X-Band CW Spectrometer. The washed $CsPbCl_3$ QDs and Mn-doped $CsPbCl_3$ QDs were dispersed in hexane and characterized at room temperature with

a modulation amplitude of 4 G and a power of 2 mW. Quinine sulfate in 0.05 M sulfuric acid was used as the reference for the relative PLQY measurements of the Mn-doped $CsPbCl_3$ QDs. The PLQY measurement was conducted in a 10 × 10 mm quartz cuvette, and all the absorption values were kept below 0.1 at the excitation wavelength (365 nm). Further information can be found in our previous studies.[47,55,56]

ACKNOWLEDGMENTS

The authors gratefully acknowledge the financial support provided by the National Science Foundation (award no. 1940959 and 1934314) and a UNC Research Opportunities Initiative (UNC-ROI) grant. This work was performed in part at the Analytical Instrumentation Facility (AIF) at North Carolina State University, which is supported by the State of North Carolina and the National Science Foundation (award no. ECCS-1542015). The AIF is a member of the North Carolina Research Triangle Nanotechnology Network (RTNN), a site in the National Nanotechnology Coordinated Infrastructure (NNCI). EPR spectroscopy was performed in part by the Molecular Education, Technology and Research Innovation Center (METRIC) at NC State University, which is supported by the State of North Carolina.

AUTHOR CONTRIBUTIONS

M.A. conceived the continuous, ultrafast metal cation-doped synthesis idea, designed the project, and coordinated the efforts of the research team. F.B. and R.W.E. contributed equally to this work. F.B. and M.A. developed the chemistry and designed the experiments. R.W.E., F.B., and M.A. developed the automated modular microfluidic platform and real-time data processing. F.B., K.A., R.D., and S.H. performed microfluidic experiments. F.B. and R.K. analyzed and processed experimental data. TEM and XRD analysis were conducted by K.A. and A.A.V. S.H. edited the supplementary video. M.R., T.C., and O.C. contributed to the cation-doping mechanism and provided feedback on the manuscript. M.A. supervised the research. All authors reviewed the manuscript and provided relevant feedback.

DECLARATION OF INTERESTS

The authors declare no conflict of interest.

Received: January 28, 2021
Revised: April 1, 2021
Accepted: April 29, 2021
Published: May 25, 2021

REFERENCES

1. Protesescu, L., Yakunin, S., Bodnarchuk, M.I., Krieg, F., Caputo, R., Hendon, C.H., Yang, R.X., Walsh, A., and Kovalenko, M.V. (2015). Nanocrystals of cesium lead halide perovskites ($CsPbX_3$, X = Cl, Br, and I): novel optoelectronic materials showing bright emission with wide color gamut. Nano Lett. *15*, 3692–3696. https://doi.org/10.1021/nl5048779.

2. Sun, S., Yuan, D., Xu, Y., Wang, A., and Deng, Z. (2016). Ligand-mediated synthesis of shape-controlled cesium lead halide perovskite nanocrystals via reprecipitation process at room temperature. ACS Nano *10*, 3648–3657. https://doi.org/10.1021/acsnano.5b08193.

3. Kovalenko, M.V., Protesescu, L., and Bodnarchuk, M.I. (2017). Properties and potential optoelectronic applications of lead halide perovskite nanocrystals. Science *358*, 745–750. https://doi.org/10.1126/science.aam7093.

4. Akkerman, Q.A., Rainò, G., Kovalenko, M.V., and Manna, L. (2018). Genesis, challenges and opportunities for colloidal lead halide perovskite nanocrystals. Nat. Mater. *17*, 394–405. https://doi.org/10.1038/s41563-018-0018-4.

5. Dong, Y., Zhao, Y., Zhang, S., Dai, Y., Liu, L., Li, Y., and Chen, Q. (2018). Recent advances toward practical use of halide perovskite nanocrystals. J. Mater. Chem. A *6*, 21729–21746. https://doi.org/10.1039/C8TA06376A.

6. Shamsi, J., Urban, A.S., Imran, M., De Trizio, L., and Manna, L. (2019). Metal halide perovskite nanocrystals: synthesis, post-synthesis modifications, and their optical properties. Chem. Rev. *119*, 3296–3348. https://doi.org/10.1021/acs.chemrev.8b00644.

7. Diroll, B.T., Nedelcu, G., Kovalenko, M.V., and Schaller, R.D. (2017). High-temperature photoluminescence of $CsPbX_3$ (X = Cl, Br, I) nanocrystals. Adv. Funct. Mater. *27*, 1606750. https://doi.org/10.1002/adfm.201606750.

8. Yang, H., Zhang, Y., Hills-Kimball, K., Zhou, Y., and Chen, O. (2018). Building bridges between halide perovskite nanocrystals and thin-film solar cells. Sustain. Energy Fuels *2*, 2381–2397. https://doi.org/10.1039/C8SE00315G.

9. Jeon, N.J., Noh, J.H., Kim, Y.C., Yang, W.S., Ryu, S., and Seok, S.I. (2014). Solvent engineering for high-performance inorganic–organic hybrid perovskite solar cells. Nat. Mater. *13*, 897–903. https://doi.org/10.1038/nmat4014.

10. Swarnkar, A., Marshall, A.R., Sanehira, E.M., Chernomordik, B.D., Moore, D.T., Christians, J.A., Chakrabarti, T., and Luther, J.M. (2016). Quantum dot-induced phase stabilization of $CsPbI_3$ perovskite for high-efficiency photovoltaics. Science *354*, 92–95. https://doi.org/10.1126/science.aag2700.

11. Liu, C., Hu, M., Zhou, X., Wu, J., Zhang, L., Kong, W., Li, X., Zhao, X., Dai, S., Xu, B., and Cheng, C. (2018). Efficiency and stability enhancement of perovskite solar cells by introducing $CsPbI_3$ quantum dots as an interface engineering layer. NPG Asia Mater. *10*, 552–561. https://doi.org/10.1038/s41427-018-0055-0.

12. Que, M., Dai, Z., Yang, H., Zhu, H., Zong, Y., Que, W., Padture, N.P., Zhou, Y., and Chen, O. (2019). Quantum-dot-induced cesium-rich surface imparts enhanced stability to formamidinium lead iodide perovskite solar cells. ACS Energy Lett. *4*, 1970–1975. https://doi.org/10.1021/acsenergylett.9b01262.

13. Zhang, Y., Yang, H., Chen, M., Padture, N.P., Chen, O., and Zhou, Y. (2019). Fusing nanowires into thin films: fabrication of graded-heterojunction perovskite solar cells with enhanced performance. Adv. Energy Mater. *29*, 1900243. https://doi.org/10.1002/aenm.201900243.

14. Li, X., Wu, Y., Zhang, S., Cai, B., Gu, Y., Song, J., and Zeng, H. (2016). $CsPbX_3$ quantum dots for lighting and displays: room-temperature synthesis, photoluminescence superiorities, underlying origins and white light-emitting diodes. Adv. Funct. Mater. *26*, 2435–2445. https://doi.org/10.1002/adfm.201600109.

15. Song, J., Li, J., Li, X., Xu, L., Dong, Y., and Zeng, H. (2015). Quantum dot light-emitting diodes based on inorganic perovskite cesium lead halides ($CsPbX_3$). Adv. Mater. *27*, 7162–7167. https://doi.org/10.1002/adma.201502567.

16. Wang, Y., Zhu, Y., Huang, J., Cai, J., Zhu, J., Yang, X., Shen, J., Jiang, H., and Li, C. (2016). $CsPbBr_3$ perovskite quantum dots-based monolithic electrospun fiber membrane as an ultrastable and ultrasensitive fluorescent sensor in aqueous medium. J. Phys. Chem. Lett. *7*, 4253–4258. https://doi.org/10.1021/acs.jpclett.6b02045.

17. Yakunin, S., Protesescu, L., Krieg, F., Bodnarchuk, M.I., Nedelcu, G., Humer, M., De Luca, G., Fiebig, M., Heiss, W., and Kovalenko, M.V. (2015). Low-threshold amplified spontaneous emission and lasing from colloidal nanocrystals of cesium lead halide perovskites. Nat. Comm. *6*, 8056. https://doi.org/10.1038/ncomms9056.

18. Ramasamy, P., Lim, D.-H., Kim, B., Lee, S.-H., Lee, M.-S., and Lee, J.-S. (2016). All-inorganic cesium lead halide perovskite nanocrystals for photodetector applications. Chem. Comm. *52*, 2067–2070. https://doi.org/10.1039/C5CC08643D.

19. Lv, L., Xu, Y., Fang, H., Luo, W., Xu, F., Liu, L., Wang, B., Zhang, X., Yang, D., Hu, W., and Dong, A. (2016). Generalized colloidal synthesis of high-quality, two-dimensional cesium lead halide perovskite nanosheets and their applications in photodetectors. Nanoscale *8*, 13589–13596. https://doi.org/10.1039/C6NR03428D.

20. Swarnkar, A., Ravi, V.K., and Nag, A. (2017). Beyond colloidal cesium lead halide perovskite nanocrystals: analogous metal halides and doping. ACS Energy Lett. *2*, 1089–1098. https://doi.org/10.1021/acsenergylett.7b00191.

21. Nedelcu, G., Protesescu, L., Yakunin, S., Bodnarchuk, M.I., Grotevent, M.J., and Kovalenko, M.V. (2015). Fast anion-exchange in highly luminescent nanocrystals of cesium lead halide perovskites ($CsPbX_3$, X = Cl, Br, I). Nano Lett. *15*, 5635–5640. https://doi.org/10.1021/acs.nanolett.5b02404.

22. Akkerman, Q.A., D'Innocenzo, V., Accornero, S., Scarpellini, A., Petrozza, A., Prato, M., and Manna, L. (2015). Tuning the optical properties of cesium lead halide perovskite nanocrystals by anion exchange reactions. J. Am. Chem. Soc. *137*, 10276–10281. https://doi.org/10.1021/jacs.5b05602.

23. Leng, M., Chen, Z., Yang, Y., Li, Z., Zeng, K., Li, K., Niu, G., He, Y., Zhou, Q., and Tang, J. (2016). Lead-free, blue emitting bismuth halide perovskite quantum dots. Angew. Chem. Int. Ed. *55*, 15012–15016. https://doi.org/10.1002/anie.201608160.

24. Zhang, Y., Liu, J., Wang, Z., Xue, Y., Ou, Q., Polavarapu, L., Zheng, J., Qi, X., and Bao, Q. (2016). Synthesis, properties, and optical applications of low-dimensional perovskites. Chem. Comm. *52*, 13637–13655. https://doi.org/10.1039/C6CC06425F.

25. Chen, D., Zhou, S., Fang, G., Chen, X., and Zhong, J. (2018). Fast room-temperature cation exchange synthesis of Mn-doped $CsPbCl_3$ nanocrystals driven by dynamic halogen exchange. ACS Appl. Mater. Interfaces *10*, 39872–39878. https://doi.org/10.1021/acsami.8b13316.

26. van der Stam, W., Geuchies, J.J., Altantzis, T., van den Bos, K.H.W., Meeldijk, J.D., Van Aert, S., Bals, S., Vanmaekelbergh, D., and de Mello Donega, C. (2017). Highly emissive divalent-ion-doped colloidal $CsPb_{1-x}M_xBr_3$ perovskite nanocrystals through cation exchange. J. Am. Chem. Soc. *139*, 4087–4097. https://doi.org/10.1021/jacs.6b13079.

27. Begum, R., Parida, M.R., Abdelhady, A.L., Murali, B., Alyami, N.M., Ahmed, G.H., Hedhili, M.N., Bakr, O.M., and Mohammed, O.F. (2017). Engineering interfacial charge transfer in $CsPbBr_3$ perovskite nanocrystals by heterovalent doping. J. Am. Chem. Soc. *139*, 731–737. https://doi.org/10.1021/jacs.6b09575.

28. Cai, T., Yang, H., Hills-Kimball, K., Song, J.-P., Zhu, H., Hofman, E., Zheng, W., Rubenstein, B.M., and Chen, O. (2018). Synthesis of all-inorganic Cd-doped $CsPbCl_3$ perovskite nanocrystals with dual-wavelength emission. J. Phys. Chem. Lett. *9*, 7079–7084. https://doi.org/10.1021/acs.jpclett.8b03412.

29. Cai, T., Wang, J., Li, W., Hills-Kimball, K., Yang, H., Nagaoka, Y., Yuan, Y., Zia, R., and Chen, O. (2020). Mn^{2+}/Yb^{3+} codoped $CsPbCl_3$ perovskite nanocrystals with triple-wavelength emission for luminescent solar concentrators. Adv. Sci. *7*, 2001317. https://doi.org/10.1002/advs.202001317.

30. Parobek, D., Roman, B.J., Dong, Y., Jin, H., Lee, E., Sheldon, M., and Son, D.H. (2016). Exciton-to-dopant energy transfer in Mn-doped cesium lead halide perovskite nanocrystals. Nano Lett. *16*, 7376–7380. https://doi.org/10.1021/acs.nanolett.6b02772.

31. Liu, W., Lin, Q., Li, H., Wu, K., Robel, I., Pietryga, J.M., and Klimov, V.I. (2016). Mn^{2+}-doped lead halide perovskite nanocrystals with dual-color emission controlled by halide content. J. Am. Chem. Soc. *138*, 14954–14961. https://doi.org/10.1021/jacs.6b08085.

32. Lin, C.C., Xu, K.Y., Wang, D., and Meijerink, A. (2017). Luminescent manganese-doped $CsPbCl_3$ perovskite quantum dots. Sci. Rep. *7*, 45906. https://doi.org/10.1038/srep45906.

33. Yuan, X., Ji, S., De Siena, M.C., Fei, L., Zhao, Z., Wang, Y., Li, H., Zhao, J., and Gamelin, D.R. (2017). Photoluminescence temperature dependence, dynamics, and quantum efficiencies in Mn^{2+}-doped $CsPbCl_3$ perovskite nanocrystals with varied dopant concentration. Chem. Mater. *29*, 8003–8011. https://doi.org/10.1021/acs.chemmater.7b03311.

34. Vlaskin, V.A., Janssen, N., van Rijssel, J., Beaulac, R., and Gamelin, D.R. (2010). Tunable dual emission in doped semiconductor nanocrystals. Nano Lett. *10*, 3670–3674. https://doi.org/10.1021/nl102135k.

35. Guria, A.K., Dutta, S.K., Adhikari, S.D., and Pradhan, N. (2017). Doping Mn^{2+} in lead halide perovskite nanocrystals: successes and challenges. ACS Energy Lett. *2*, 1014–1021. https://doi.org/10.1021/acsenergylett.7b00177.

36. Mir, W.J., Jagadeeswararao, M., Das, S., and Nag, A. (2017). Colloidal Mn-doped cesium lead halide perovskite nanoplatelets. ACS Energy Lett. *2*, 537–543. https://doi.org/10.1021/acsenergylett.6b00741.

37. Zhou, S., Zhu, Y., Zhong, J., Tian, F., Huang, H., Chen, J., and Chen, D. (2019). Chlorine-additive-promoted incorporation of Mn^{2+} dopants into $CsPbCl_3$ perovskite nanocrystals. Nanoscale *11*, 12465–12470. https://doi.org/10.1039/C9NR04663A.

38. Gao, D., Qiao, B., Xu, Z., Song, D., Song, P., Liang, Z., Shen, Z., Cao, J., Zhang, J., and Zhao, S. (2017). Postsynthetic, reversible cation exchange between Pb^{2+} and Mn^{2+} in cesium lead chloride perovskite nanocrystals. J. Phys. Chem. C *121*, 20387–20395. https://doi.org/10.1021/acs.jpcc.7b06929.

39. Zhu, J., Yang, X., Zhu, Y., Wang, Y., Cai, J., Shen, J., Sun, L., and Li, C. (2017). Room-temperature synthesis of Mn-doped cesium lead halide quantum dots with high Mn substitution ratio. J. Phys. Chem. Lett. *8*, 4167–4171. https://doi.org/10.1021/acs.jpclett.7b01820.

Please cite this article in press as: Bateni et al., Ultrafast cation doping of perovskite quantum dots in flow, Matter (2021), https://doi.org/10.1016/j.matt.2021.04.025

40. Nag, A., Chakraborty, S., and Sarma, D.D. (2008). To dope Mn^{2+} in a semiconducting nanocrystal. J. Am. Chem. Soc. *130*, 10605–10611. https://doi.org/10.1021/ja801249z.

41. Huang, G., Wang, C., Xu, S., Zong, S., Lu, J., Wang, Z., Lu, C., and Cui, Y. (2017). Postsynthetic doping of $MnCl_2$ molecules into preformed $CsPbBr_3$ perovskite nanocrystals via a halide exchange-driven cation exchange. Adv. Mater. *29*, 1700095. https://doi.org/10.1002/adma.201700095.

42. Hills-Kimball, K., Pérez, M.J., Nagaoka, Y., Cai, T., Yang, H., Davis, A.H., Zheng, W., and Chen, O. (2020). Ligand engineering for Mn^{2+} doping control in $CsPbCl_3$ perovskite nanocrystals via a quasi-solid–solid cation exchange reaction. Chem. Mater. *32*, 2489–2500. https://doi.org/10.1021/acs.chemmater.9b05082.

43. Abdel-Latif, K., Bateni, F., Crouse, S., and Abolhasani, M. (2020). Flow synthesis of metal halide perovskite quantum dots: from rapid parameter space mapping to AI-guided modular manufacturing. Matter *3*, 1053–1086. https://doi.org/10.1016/j.matt.2020.07.024.

44. Campbell, Z.S., Bateni, F., Volk, A.A., Abdel-Latif, K., and Abolhasani, M. (2020). Microfluidic synthesis of semiconductor materials: toward accelerated materials development in flow. Part. Part. Syst. Charact. *37*, 2000256. https://doi.org/10.1002/ppsc.202000256.

45. Volk, A.A., Epps, R.W., and Abolhasani, M. (2020). Accelerated development of colloidal nanomaterials enabled by modular microfluidic reactors: toward autonomous robotic experimentation. Adv. Mater. *33*, 2004495. https://doi.org/10.1002/adma.202004495.

46. Vikram, A., Zahid, A., Bhargava, S.S., Jang, H., Sutrisno, A., Khare, A., Trefonas, P., Shim, M., and Kenis, P.J.A. (2020). Unraveling the origin of interfacial oxidation of InP-based quantum dots: implications for bioimaging and optoelectronics. ACS Appl. Nano Mater. *3*, 12325–12333. https://doi.org/10.1021/acsanm.0c02814.

47. Abdel-Latif, K., Epps, R.W., Kerr, C.B., Papa, C.M., Castellano, F.N., and Abolhasani, M. (2019). Facile room-temperature anion exchange reactions of inorganic perovskite quantum dots enabled by a modular microfluidic platform. Adv. Funct. Mater. *29*, 1900712. https://doi.org/10.1002/adfm.201900712.

48. Epps, R.W., Felton, K.C., Coley, C.W., and Abolhasani, M. (2017). Automated microfluidic platform for systematic studies of colloidal perovskite nanocrystals: towards continuous nano-manufacturing. Lab. Chip *17*, 4040–4047. https://doi.org/10.1039/C7LC00884H.

49. Abdel-Latif, K., Epps, R.W., Bateni, F., Han, S., Reyes, K.G., and Abolhasani, M. (2020). Self-driven multistep quantum dot synthesis enabled by autonomous robotic experimentation in flow. Adv. Intell. Syst. *3*, 2000245. https://doi.org/10.1002/aisy.202000245.

50. Lignos, I., Stavrakis, S., Nedelcu, G., Protesescu, L., deMello, A.J., and Kovalenko, M.V. (2016). Synthesis of cesium lead halide perovskite nanocrystals in a droplet-based microfluidic platform: fast parametric space mapping. Nano Lett. *16*, 1869–1877. https://doi.org/10.1021/acs.nanolett.5b04981.

51. Maceiczyk, R.M., Dümbgen, K., Lignos, I., Protesescu, L., Kovalenko, M.V., and deMello, A.J. (2017). Microfluidic reactors provide preparative and mechanistic insights into the synthesis of formamidinium lead halide perovskite nanocrystals. Chem. Mater. *29*, 8433–8439. https://doi.org/10.1021/acs.chemmater.7b02998.

52. Liang, X., Baker, R.W., Wu, K., Deng, W., Ferdani, D., Kubiak, P.S., Marken, F., Torrente-Murciano, L., and Cameron, P.J. (2018). Continuous low temperature synthesis of $MAPbX_3$ perovskite nanocrystals in a flow reactor. React. Chem. Eng. *3*, 640–644. https://doi.org/10.1039/C8RE00098K.

53. Lignos, I., Morad, V., Shynkarenko, Y., Bernasconi, C., Maceiczyk, R.M., Protesescu, L., Bertolotti, F., Kumar, S., Ochsenbein, S.T., Masciocchiet, N., et al. (2018). Exploration of near-infrared-emissive colloidal multinary lead halide perovskite nanocrystals using an automated microfluidic platform. ACS Nano *12*, 5504–5517. https://doi.org/10.1021/acsnano.8b01122.

54. Lignos, I., Protesescu, L., Emiroglu, D.B., Maceiczyk, R., Schneider, S., Kovalenko, M.V., and deMello, A.J. (2018). Unveiling the shape evolution and halide-ion-segregation in blue-emitting formamidinium lead halide perovskite nanocrystals using an automated microfluidic platform. Nano Lett. *18*, 1246–1252. https://doi.org/10.1021/acs.nanolett.7b04838.

55. Epps, R.W., Bowen, M.S., Volk, A.A., Abdel-Latif, K., Han, S., Reyes, K.G., Amassian, A., and Abolhasani, M. (2020). Artificial chemist: an autonomous quantum dot synthesis bot. Adv. Mater. *32*, 2001626. https://doi.org/10.1002/adma.202001626.

56. Epps, R.W., Volk, A.A., Abdel-Latif, K., and Abolhasani, M. (2020). An automated flow chemistry platform to decouple mixing and reaction times. React. Chem. Eng. *5*, 1212–1217. https://doi.org/10.1039/D0RE00129E.

57. Sui, J., Yan, J., Liu, D., Wang, K., and Luo, G. (2020). Continuous synthesis of nanocrystals via flow chemistry technology. Small *16*, 1902828. https://doi.org/10.1002/smll.201902828.

58. Khan, S.A., and Jensen, K.F. (2007). Microfluidic synthesis of titania shells on colloidal silica. Adv. Mater. *19*, 2556–2560. https://doi.org/10.1002/adma.200700127.

59. Cambié, D., Bottecchia, C., Straathof, N.J.W., Hessel, V., and Noël, T. (2016). Applications of continuous-flow photochemistry in organic synthesis, material science, and water treatment. Chem. Rev. *116*, 10276–10341. https://doi.org/10.1021/acs.chemrev.5b00707.

60. Marre, S., and Jensen, K.F. (2010). Synthesis of micro and nanostructures in microfluidic systems. Chem. Soc. Rev. *39*, 1183. https://doi.org/10.1039/b821324k.

61. Kerr, C.B., Epps, R.W., and Abolhasani, M. (2019). A low-cost, non-invasive phase velocity and length meter and controller for multiphase lab-in-a-tube devices. Lab. Chip *19*, 2107–2113. https://doi.org/10.1039/C9LC00296K.

62. Epps, R.W., Felton, K.C., Coley, C.W., and Abolhasani, M. (2018). A modular microfluidic technology for systematic studies of colloidal semiconductor nanocrystals. J. Vis. Exp. *135*, e57666. https://doi.org/10.3791/57666.

63. Sebastian Cabeza, V., Kuhn, S., Kulkarni, A.A., and Jensen, K.F. (2012). Size-controlled flow synthesis of gold nanoparticles using a segmented flow microfluidic platform. Langmuir *28*, 7007–7013. https://doi.org/10.1021/la205131e.

64. Chen, D.L., Li, L., Reyes, S., Adamson, D.N., and Ismagilov, R.F. (2007). Using three-phase flow of immiscible liquids to prevent coalescence of droplets in microfluidic channels: criteria to identify the third liquid and validation with protein crystallization. Langmuir *23*, 2255–2260. https://doi.org/10.1021/la062152z.

65. Zheng, B., and Ismagilov, R.F. (2005). A microfluidic approach for screening submicroliter volumes against multiple reagents by using preformed arrays of nanoliter plugs in a three-phase liquid/liquid/gas flow. Angew. Chem. Int. Ed. *44*, 2520–2523. https://doi.org/10.1002/anie.200462857.

66. Milstein, T.J., Kroupa, D.M., and Gamelin, D.R. (2018). Picosecond quantum cutting generates photoluminescence quantum yields over 100% in ytterbium-doped $CsPbCl_3$ nanocrystals. Nano Lett. *18*, 3792–3799. https://doi.org/10.1021/acs.nanolett.8b01066.

67. Ravi, V.K., Markad, G.B., and Nag, A. (2016). Band edge energies and excitonic transition probabilities of colloidal $CsPbX_3$ (X = Cl, Br, I) perovskite nanocrystals. ACS Energy Lett *1*, 665–671. https://doi.org/10.1021/acsenergylett.6b00337.

68. Zheng, X., Hou, Y., Sun, H.-T., Mohammed, O.F., Sargent, E.H., and Bakr, O.M. (2019). Reducing defects in halide perovskite nanocrystals for light-emitting applications. J. Phys. Chem. Lett. *10*, 2629–2640. https://doi.org/10.1021/acs.jpclett.9b00689.

69. De, A., Mondal, N., and Samanta, A. (2017). Luminescence tuning and exciton dynamics of Mn-doped $CsPbCl_3$ nanocrystals. Nanoscale *9*, 16722–16727. https://doi.org/10.1039/C7NR06745C.

70. DasAdhikari, S., Dutta, S.K., Dutta, A., Guria, A.K., and Pradhan, N. (2017). Chemically tailoring the dopant emission in manganese-doped $CsPbCl_3$ perovskite nanocrystals. Angew. Chem. Int. Ed. *56*, 8746–8750. https://doi.org/10.1002/anie.201703863.

71. Bodnarchuk, M.I., Boehme, S.C., ten Brincket, S., Bernasconi, C., Shynkarenko, Y., Krieg, F., Widmer, R., Aeschlimann, B., Günther, D., Kovalenko, M.V., and Infante, I. (2019). Rationalizing and controlling the surface structure and electronic passivation of cesium lead halide nanocrystals. ACS Energy Lett. *4*, 63–74. https://doi.org/10.1021/acsenergylett.8b01669.

72. De Roo, J., Ibáñez, M., Geiregat, P., Nedelcu, G., Walravens, W., Maes, J., Martins, J.C., Van Driessche, I., Kovalenko, M.V., and Hens, Z. (2016). Highly dynamic ligand binding and light absorption coefficient of cesium lead bromide perovskite nanocrystals. ACS Nano *10*, 2071–2081. https://doi.org/10.1021/acsnano.5b06295.